RSC Advances

PAPER

View Article Online
View Journal | View Issue

Cite this: *RSC Adv.*, 2016, **6**, 28149

Structure and chemistry of surface-doped Pt:SnO_2 gas sensing materials†

David Degler,[a] Hudson W. Pereira de Carvalho,[bc] Kristina Kvashnina,[de] Jan-Dierk Grunwaldt,[b] Udo Weimar[a] and Nicolae Barsan*[a]

Received 9th December 2015
Accepted 7th March 2016

DOI: 10.1039/c5ra26302f

www.rsc.org/advances

Surface-doped Pt:SnO_2 was synthesized by impregnation of calcined SnO_2 made by an aqueous sol–gel route. The structure of the introduced Pt-dopant and its behaviour during gas exposure were examined by *in situ* and operando X-ray absorption spectroscopy. The results reveal that Pt forms a nano-sized PtO_2 phase, which was not found for bulk and surface doped materials, studied previously. In a comparative investigation of undoped and Pt-doped SnO_2 gas sensors the performance and the surface chemistry were investigated, the latter one using operando FT-IR spectroscopy. The results prove the strong influence of the different Pt structures on the surface chemistry of SnO_2, providing the basis for an understanding on the varying sensor performance of differently synthesized Pt:SnO_2 gas sensing materials.

1. Introduction

Gas sensors based on semiconducting metal oxides, first and foremost SnO_2, are widely used for the detection of flammable and toxic gases such as CO, H_2 or CH_4.[1,2] Under typical gas sensing conditions – high background humidity and the presence of interfering gases – pure SnO_2 materials show a strongly decreased sensor signal, sensitivity and stability. In order to overcome this disadvantage noble metals like Pd[3–12] or Pt[3,5,13–18] are added to SnO_2, changing its surface chemistry and/or electrical properties.[17,18] Previous studies have shown, that already small differences in the introduction method of the noble metal, (doping before or after calcination, calcination temperature or noble metal concentration) lead to very different dopant structures and thus gas sensing properties.[3,5,19,20] However, these results were obtained by *ex situ* techniques, like photoelectron spectroscopy or electron microscopy, and the derived structural parameters can thus not be directly applied to explain the effect of noble metal doping during gas sensing.[21,22] An improved approach to understand the role of noble metals in gas sensing materials is the use of operando spectroscopic techniques which allow the examination of gas sensors under operating conditions. X-ray absorption spectroscopy (XAS) has been proven to be a suitable operando techniques to study structural parameters of even low concentrated noble metals (0.2% wt) in gas sensing materials, by interpretation of the extended X-ray absorption fine structure (EXAFS), and the behaviour of the noble metal in various atmospheric conditions, mainly obtained by the analysis of the X-ray absorption near edge structure (XANES).[23–25] Complementary to the structural evaluation the surface chemistry of gas sensing layers can be studied by operando diffuse reflectance infrared Fourier-transform spectroscopy (DRIFTS), revealing surface species actively interacting with or caused by the atmosphere, such as carbonylic species on the noble metal surface, carbonates, hydroxyls or M–O overtones on SnO_2, which are considered to be fundamental for understanding the gas reception mechanism.[9,22,26–28] The potential of these methods was demonstrated when examining SnO_2:Pt which was doped before the final calcination steps.[20] The structural evaluation by XAS showed that Pt replaces Sn^{4+} ions in the SnO_2 lattice and that it is atomically distributed on the surface and in the bulk of the whole material.[29] As observed by DRIFTS the atomically distributed Pt^{4+} sites change the chemistry of hydrogen containing gases (H_2, H_2O) and hence improve the CO sensing performance of this material.[13] Furthermore, it was shown that Pt^{4+} in the bulk of the material has a strong influence on the electrical properties of the SnO_2 and consequently the improved gas sensing properties were traced back to changes in the chemistry and the electronic properties of the material.[30] This raises the question which effect Pt exhibits on SnO_2 if it is only present on the surface of the material.

[a]*University of Tübingen, Institute of Physical and Theoretical Chemistry, Auf der Morgenstelle 15, 72076 Tübingen, Germany. E-mail: nb@ipc.uni-tuebingen.de; Tel: +49 7071 29 78761*

[b]*Karlsruhe Institute of Technology, Institute for Chemical Technology and Polymer Chemistry, Engesserstr. 20, 76131 Karlsruhe, Germany*

[c]*Centro de Energia Nuclear na Agricultura, Universidade de São Paulo, P. O. Box 96, 13400-970, Piracicaba, SP, Brazil*

[d]*ESRF, BP220, 6 rue Jules Horowitz, 38043 Grenoble, France*

[e]*Helmholtz-Zentrum Dresden-Rossendorf (HZDR), Institute of Resource Ecology, P. O. Box 510119, 01314, Dresden, Germany*

† Electronic supplementary information (ESI) available: (i) Refined fitted EXAFS spectra of PtO_2 (reference) and SnO_2 (reference). See DOI: 10.1039/c5ra26302f

2. Experimental

2.1. Sample preparation

Undoped tin dioxide was synthesized by an aqueous sol–gel route starting with $SnCl_4$ (Merck, purified by distillation). The precipitated solid was separated, washed several times, dried (120 °C), calcined at 1000 °C for 8 h under air and milled afterwards. The Pt loadings were introduced either before the calcination step (gel-impregnation, GI) or after the calcination step (powder-impregnation, PI) as an aqueous solution of H_2PtCl_6 ($PtCl_4$, Aldrich, ≥99.99% trace metal basis) added to the SnO_2 suspension and stirred for 48 h at room temperature. The PI material was additionally thermally treated after the impregnation (450 °C, 1 h). The prepared doped materials aimed at a nominal Pt loading of 0.2% wt. Gas sensors were made by screen printing a paste, made from undoped or Pt-doped SnO_2 powders and an organic binder (propandiol), on alumina substrates equipped with interdigitated electrodes and a backside heating meander.[31] Pt-Electrodes and Pt-heaters were used for gas sensor characterization by DC-resistance measurements and IR spectroscopy. For the X-ray spectroscopic analysis of the Pt-doped sample alumina substrates with Au-electrodes and an Ag/Pd-alloy-heater were used to avoid interference of Pt signals (absorption/fluorescence) from the substrates during XAS measurements.

2.2. General experimental setup

For all experiments similar basic setups were used, allowing to control the atmospheric composition, the temperature of the sensor and the readout of the sensor response.[22] Gases were mixed using home-made gas mixing stations based on mass flow controllers (Bronkhorst EL-Flow select). Test gases mixtures (H_2 in synthetic air or He) were added to a carrier gas stream (synthetic air or He). Humidity levels were dosed by using evaporators filled with deionized water. The sensors were heated by applying voltage and current to the backside heaters using a DC-powder supply (Agilent E 3630A) and adjusting the exact values according to the sensor's temperature calibration. All experiments were conducted at 300 °C if not specified differently. To characterize the sensor responses as such and during all operando spectroscopic experiments the resistance was measured using a digital multimeter (Keithley 2000). All experiments were performed by measuring one sensor at a time to avoid downstream effects, which are expected for Pt-doped SnO_2 gas sensors.[15]

2.3. Operando X-ray absorption spectroscopy

In situ and operando high-energy-resolution fluorescence detected (HERFD) X-ray absorption spectroscopy measurements were performed at beamline ID26 at the European Synchrotron Radiation Facility (ESRF, Grenoble, France). At this experimental station the beam was provided by a set of mechanically independent undulators. The incident energy was selected by a Si (111) double crystal monochromator. The beam size on the sample had an area 0.2 × 0.5 mm^2 (vertical × horizontal) and the energy calibration was performed using a Pt foil. The spectra were recorded in high-energy-resolution fluorescence detection by means of an X-ray emission spectrometer. The sample, analyzer crystals and avalanche photodiode were displaced in a vertical Rowland geometry. The Pt L_3-edge HERFD spectra were measured recording the intensity of the Pt Lα1 emission line (9442 eV) as a function of the incident energy. The emission energy was selected using the ⟨660⟩ reflection of four spherically bent Ge crystal analyzers. The broadening of the elastic peak was 1.8 eV. The sensors were mounted in a special home-made cell which allowed recording both HERFD spectra and electrical resistance as function of the atmosphere composition and temperature.[24] XAS data analysis was carried out using Athena and Arthemis software of the IFEFFIT package.[32] The spectra were energy calibrated, background subtracted and then normalized. The structural parameters were obtained by adjusting theoretical structural models, *ab initio* calculated phase and amplitude functions using the FEFF 6.0 code,[33] to the experimental data. The EXAFS spectra in *k* space were Fourier transformed between 3.0 and 11.5 $Å^{-1}$ and the data fitting was performed in *R* space between 1.0 and 2.2 Å for the first coordination shell, and between 1 and 4 Å when further shells were considered. The number of fitted parameters was always lower than the number of independent ones.

The ratio between the oxidized and reduced Pt species were estimated by linear combination fitting (LCF) of operando XANES spectra using Athena IFEFFIT.[32] The linear combination fitting was performed in the spectral range of −20 and 70 eV referred to the absorption edge. This procedure allowed tracking the proportion of oxidized and reduced Pt species. Since the references for the linear combinations were the first spectrum of the series and a spectrum of a Pt foil (both recorded at room temperature) the calculated ratios are relative values.

2.4. Operando DRIFT spectroscopy

Operando FT-IR spectroscopy was done on a Bruker Vertex70v spectrometer equipped with an external high performance globar, a KBr beamsplitter and a mid-band MCT detector. All samples were measured in diffuse reflectance geometry using a mirror optic (Praying Mantis, Harrick) with a home-made operando cell placed inside, which allows simultaneous resistance and spectroscopic measurements.[9] Single channel spectra were recorded averaging 512 scans with a spectral resolution of 1 cm^{-1}. The as obtained single channel spectra were processed with Bruker's OPUS software (version 7.2). Absorbance spectra were calculated as apparent absorbance using a single channel spectrum of the sensor before test gas exposure as reference.[9,28]

3. Results

3.1. Gas sensing performance

Fig. 1 shows the sensor signals to CO of undoped and Pt-doped materials in dry and humid air. Considering first the sensor performance in dry air (empty symbols) the undoped material shows the highest sensor signals to CO, followed by Pt:SnO_2 GI, while Pt:SnO_2 PI shows the lowest sensor signals. However, in the presence of water vapour (filled symbols) the situation

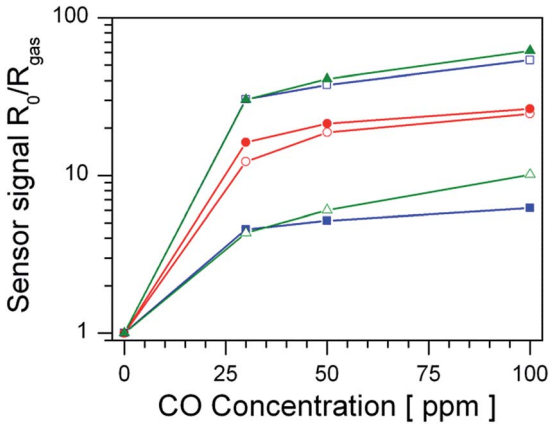

Fig. 1 Sensor signals of undoped SnO_2 (blue squares), Pt:SnO_2 GI (red circles) and Pt:SnO_2 PI (green triangles) in dry (empty symbols) and humid (50% r.h. at 25 °C, filled symbols) air.

changes: the undoped material shows a substantial decrease of the sensor signals compared to dry air, while the sensor signals of Pt:SnO_2 PI are strongly increased. The Pt:SnO_2 GI sensor shows only a minor increase, compared to the one observed for Pt:SnO_2 PI. In order to understand these findings, the differences in the structure of the platinum dopant and the resulting changes of the materials chemistry have to be studied.

3.2. Structural investigations

As basis for understanding the effect of Pt surface doping the structure, oxidation state and dispersion of Pt need to be unravelled. For GI materials a detailed XAS investigation has reported by M. Hübner *et al.*,[25] showing that Pt replaces Sn^{4+} ions in the SnO_2 lattice and that it is distributed in the whole material.[25] Similar results were recently reported by N. Murata *et al.*,[16] finding a up to 10% at of Pt incorporated in SnO_2. Hence, the following section focuses on the PI material. Fig. 2 presents the Fourier-transform of *ex situ* recorded EXAFS spectra of PtO_2 (bulk) reference and Pt:SnO_2 PI. The peaks shown in Fig. 2 are related to the backscattering of the nearest neighbours and thus the atomic radial distribution function (not phase-shifted) around the Pt absorber atoms. The visual inspection already reveals that the first coordination shell around the Pt atoms of PtO_2 and Pt:SnO_2 PI is the same, while the outer backscattering contributions (2nd and 3rd peak) are dissimilar. This indicates that the Pt dopant in SnO_2 forms a PtO_2-like phase which has not completely the same structure like the bulk oxide (PtO_2). Quantitative structural information was obtained by fitting theoretical calculated spectra to the experimental ones; the structural parameters are presented in Table 1 and the refined spectra of the experimental data and the reference materials are shown in Fig. 3 and ESI 1 to 2,† respectively. The first hypothetical structural model considered that the chemical environment of Pt atoms in Pt:SnO_2 PI is similar to one found in PtO_2, this approach was satisfactory to describe the first coordination shell; however it failed to fit to the outer shells. The Pt atoms in SnO_2:Pt presented 6.0 oxygen atoms at 2.02 Å, it means that coordination number and distance fits to the values observed for PtO_2 bulk reference. Interestingly, the mean-square deviation of interatomic distances (σ^2) is considerably higher for the sensing material than for the reference bulk oxide. This parameter accounts for the structural disorder, at low temperatures it expresses that static disorder of the pair distribution function and at high temperatures it reveals the thermal disorder summed to the static one. As long as all *ex situ* measurements were carried out at room temperature, the high σ^2 suggest that Pt atoms in the sensor powder are in disordered environment that could result from the low particle size. To describe the outer shells FEFF 6.0 generated paths from PtO_2 and SnO_2 models were used. A constraint was applied to the second coordination forcing the number of neighbours to be ≤6 like it was found for PtO_2. The analysis shows that Sn atoms are required to fit the model to the experimental spectra. Pt:SnO_2 PI presents Pt neighbours at 3.14 ± 0.05 Å and Sn atoms at 3.63 ± 0.03 Å. This differs from the previous study were Pt was introduced before the calcination step: in this study the 2nd coordination shell contained only Sn atoms; this was interpreted as an atomic distribution of Pt, replacing Sn atoms in the SnO_2 lattice.[25] The EXAFS analysis of

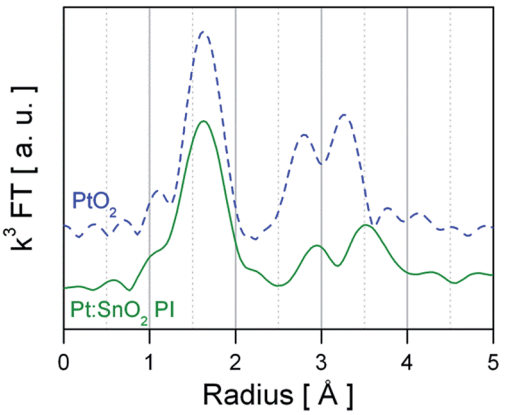

Fig. 2 k^3 weighted Fourier transform of *ex situ* recorded EXAFS spectra from reference PtO_2 (blue dashed line) and SnO_2:Pt (green straight line).

Table 1 Parameters obtained from EXAFS analysis of the measured SnO_2:Pt PI and reference materials PtO_2 (ESI 1) and SnO_2 (ESI 2)[a]

	Atom	N	R [Å]	σ^2 [10^{-3} Å^2]	ρ [%]
SnO_2:Pt PI	O	6.0[f]	2.02 ± 0.01[a]	3.1 ± 0.1[a]	4.7
	Pt	2.4 ± 1.4[c]	3.14 ± 0.05[a]	4.8 ± 3.0[a]	
	Sn	3.6 ± 1.4[c]	3.63 ± 0.03[a]	4.8 ± 3.0[a]	
PtO_2	O	6.0[f]	2.02 ± 0.01[a]	2.7 ± 0.9[a]	4.5
	Pt	6.0[f]	3.10 ± 0.01[a]	2.7 ± 0.5[a]	
SnO_2	O	6.0[f]	2.06 ± 0.02[a]	3.1 ± 0.4[a]	1.0
	Sn	2.0[f]	3.21 ± 0.02[a]	5.2 ± 0.2[a]	
	O	4.0[f]	3.60 ± 0.02[a]	4.1 ± 3.0[a]	
	Sn	8.0[f]	3.73 ± 0.02[a]	4.0 ± 0.2[a]	

[a] PtO_2: $\Delta E_0 = 12.9 \pm 1.0$ eV, SnO_2:Pt: $\Delta E_0 = 12.7 \pm 1.7$ eV SnO_2: $\Delta E_0 = 5.4 \pm 0.5$ eV; Sn K $S_o^2 = 1.07$, Pt L_3 $S_o^2 = 0.83$; a = adjusted; f = fixed; c = constrained.

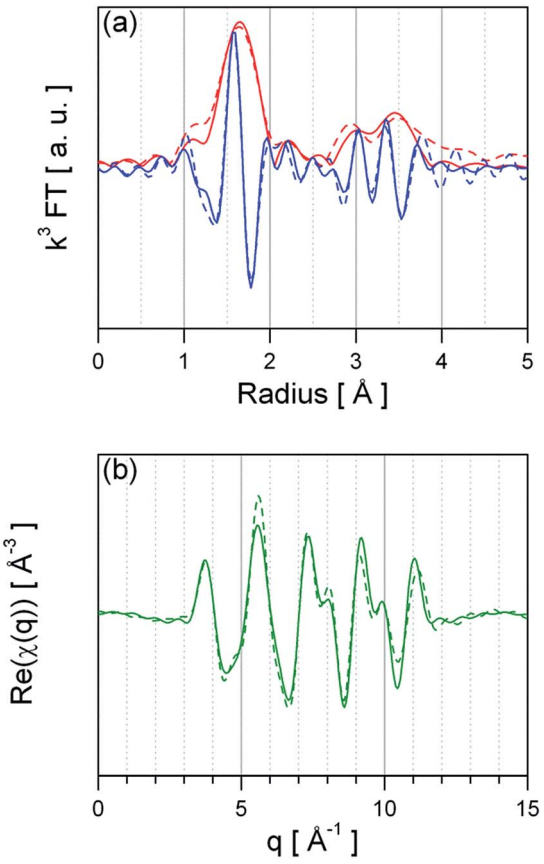

Fig. 3 Real part (a) and imaginary part (b) of the refined EXAFS fits of Pt:SnO_2 PI. The dashed line represents the experimental data and the solid line the fit function.

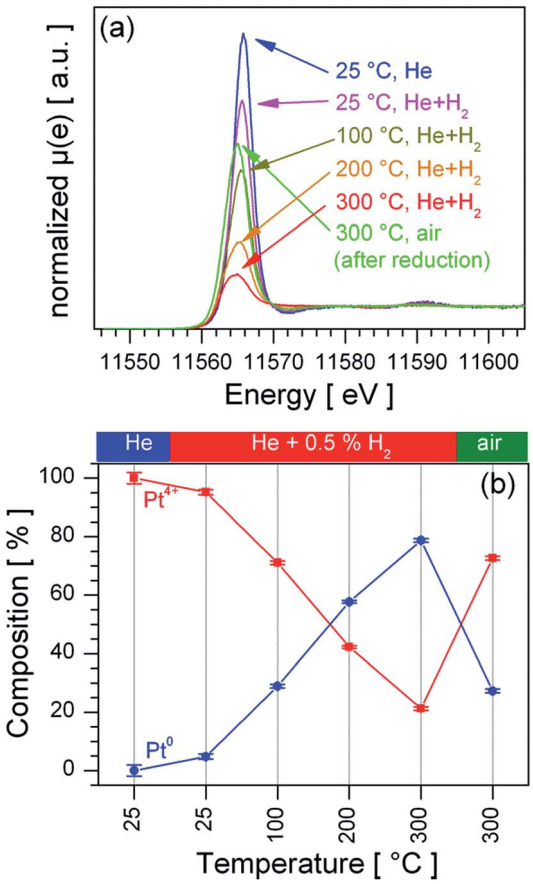

Fig. 4 TPR-XANES spectra recorded from Pt:SnO_2 PI sensor in different conditions (a) and the corresponding LCF calculations (b). In (b) the circles and line show the concentration of Pt^{4+}, while the concentration of Pt^0 is represented by the blue circles and line.

Pt:SnO_2 PI has to be interpreted as the formation of a nano-sized PtO_2 phase on the surface or inside of the SnO_2 material.

To determine the distribution of the Pt dopant temperature programmed reduction (TPR) was performed on a stepwise heated sensor in a 0.5% vol. H_2/He atmosphere, the recorded XANES spectra (Fig. 4a) were quantitatively analysed by LCF analysis, as shown in Fig. 4b. The Pt:SnO_2 PI material is already reduced at room temperature in 0.5% vol. H_2/He; the stepwise increase of the sensor's temperature leads to a further reduction of the Pt, which ends in the formation of a mainly metallic Pt at 300 °C. Switching from the reducing atmosphere to synthetic air causes a re-oxidation of the Pt at 300 °C. Since the re-oxidation is a slow process it did not reach the initial Pt composition in the time allotted to the re-oxidation experiment (90 minutes). In contrast Pt:SnO_2 GI is only partially reduced under much harsher conditions (2% vol. H_2/He at 600 °C, see ESI 3†). The clear difference in the reducibility of Pt for the two samples points out that for Pt:SnO_2 PI the Pt is accessible to gases, *i.e.* only present at the surface and not incorporated in the SnO_2 lattice. The Pt oxidation state strongly depends on the composition of the atmosphere, *i.e.* the Pt actively interacts with reducing and oxidizing gases.

The structural evaluation presented above revealed that powder-impregnation leads to the formation of a nano-sized PtO_2 phase mostly present at the surface of SnO_2 (Fig. 5a), which strongly differs from the structure Hübner *et al.*[25] proposed for gel-impregnated materials, for which Pt is atomically dispersed in the SnO_2 bulk and surface (Fig. 5b). A similar occurrence of atomically distributed Pd or a separate oxide phase is observed when comparing Pd-doped SnO_2 materials

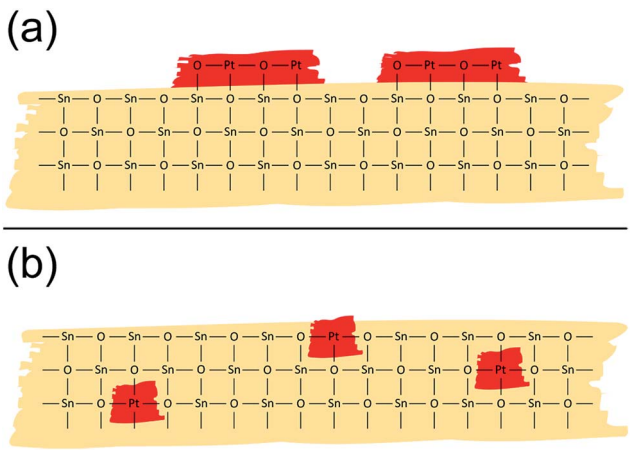

Fig. 5 Schematic representation of the Pt structure as proposed by EXAFS and XANES analysis for Pt:SnO_2 PI (a) and Pt:SnO_2 GI (b).

made by gel-impregnation or flame spray pyrolysis (dopant introduced before/during the grain formation) with powder-impregnated materials (dopant introduced after the grain formation).[4,24]

3.3. Operando XAS

The fundamental models for the enhanced gas sensing performance of noble metal loaded SnO_2 are closely linked to the oxidation state of the noble metal: for metallic clusters a chemical sensitization by a spill-over mechanism is expected, while for partial oxidized clusters – being reduced during test gas exposure – an electronic sensitization by the alignment of the Fermi-levels is a commonly accepted model.[17,18] Hence, the oxidation state of Pt under operation conditions is of fundamental interest to understand the role of Pt for gas sensing. Since the TPR experiments showed that PtO_2 phase is easily reduced and re-oxidized at 300 °C the question raises which oxidation state of Pt is dominant under operation conditions in the absence and presence of H_2. Fig. 6 shows XANES recorded from heated sensors in dry air and dry air containing 50 ppm H_2. For both materials the presence of H_2 leads to a slight decrease of the white line (first absorption feature above the Pt L_3 edge), which indicates a weak reduction of the Pt, but for none of the materials a shift or strong decrease of the white line, which indicates the formation of metallic Pt, is observed. In the case of Pt:SnO_2 PI the lack of a considerable reduction can be explained with the high excess of O_2 – 20.5% O_2 in comparison with 50 ppm H_2 – which favours the re-oxidation and prevents the formation of a metallic Pt phase under operating conditions. As Pt:SnO_2 GI is not reducible even at higher H_2 concentrations and in the absence of oxygen, it is expected that it is not reduced by very low H_2 concentration in air. The XAS spectra shown in Fig. 6 do not show any differences between Pt:SnO_2 PI and GI, *i.e.* for both materials oxidized Pt dominates under operating conditions.

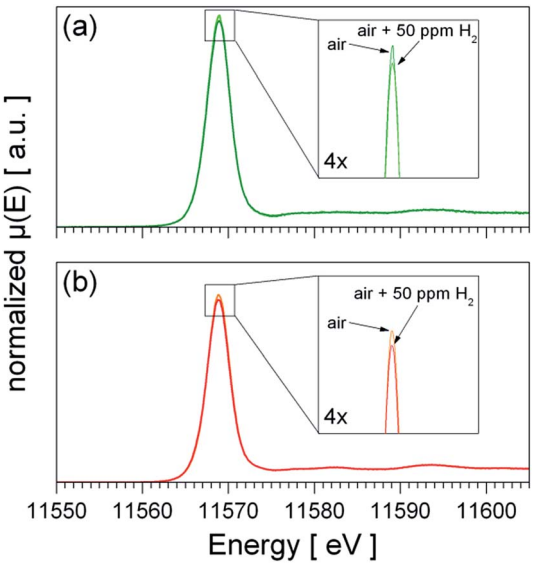

Fig. 6 Operando XANES spectra of Pt:SnO_2 PI (a) and Pt:SnO_2 GI (b) recorded at 300 °C in dry air and dry air plus 50 ppm H_2. The spectra shown in (b) is based on the raw data measured by M. Hübner *et al.*[25] and was treated similar to the data shown in (a).

3.4. Operando DRIFTS

Pt-based catalysts are widely used for the catalytic oxidation of CO.[34,35] Oxidized[36–40] as well as reduced[35,41–44] Pt species are reported to be catalytically active, whereupon the latter one is found to be more reactive.[41,42] Thus it is reasonable to assume that Pt, in either form, chemically sensitizes the SnO_2 material and that such a chemical sensitization should result in a changed surface chemistry, as it was demonstrated for Pt:SnO_2 GI.[13]

Fig. 7 shows DRIFT spectra of both Pt-doped materials recorded during CO exposure in dry and humid air. In agreement with previous works undoped SnO_2 shows no carbonyl species under operation conditions (spectra not shown).[45] During CO exposure both Pt-doped samples (Fig. 7a and b) show the formation of different carbonyl species; due to the absence of carbonyls on undoped SnO_2, these carbonyls are identified as platinum carbonyl species (Pt–CO). On both materials only carbonyl species assigned to oxidized platinum are observed, while no carbonyl bands on metallic Pt can be assigned.[46] This supports the findings by operando XAS, which did not show the formation of metallic Pt under operation conditions. A closer look reveals, that Pt:SnO_2 PI shows two carbonyl species at 2148 and 2131 or 2135 cm^{-1} (Fig. 7a), while Pt:SnO_2 GI shows only one carbonyl species at 2124 cm^{-1} (Fig. 7b). Again this is in line with the structure proposed for both materials: in case of Pt:SnO_2 PI the presence of PtO_2 clusters offers a higher heterogeneity of Pt-sites – *e.g.* edges and planar surface regions – available for CO adsorption; which is in line with the appearance of several different carbonyl species. In case of Pt:SnO_2 GI the atomically distributed Pt should be found in a homogeneous surrounding, which is in line with the appearance of a single carbonyl species.

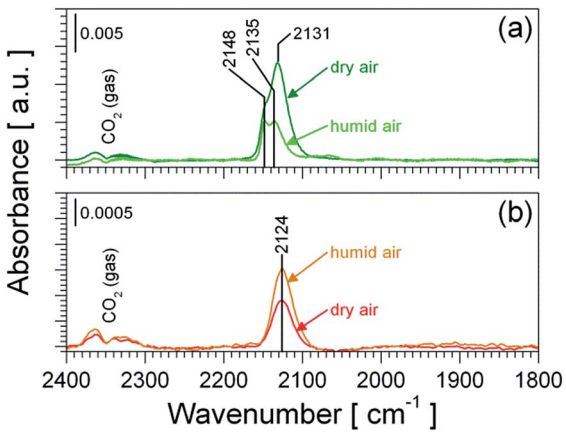

Fig. 7 Operando DRIFT spectra of Pt:SnO_2 PI (a) and Pt:SnO_2 GI (b) recorded during the exposure of 100 ppm CO in dry air (reference: dry air) and humid air (reference: humid air) at 300 °C. The spectra shown in (b) are based on the experimental data previously published by K. Großmann *et al.*[13]

Since the carbonyls on Pt:SnO_2 PI appear at higher wavenumbers than the carbonyl species on Pt:SnO_2 GI (see Fig. 7) an incorporation of Pt into the SnO_2, as it is observed for Pt:SnO_2 GI, can be ruled out; again this is in line with XAS results. Consequently, the occurrence of carbonyl species on the Pt-doped samples point out that the sensitization caused by Pt-doping is related to changed chemistry, which is linked closely to the structure of the Pt doping. Regarding the effect of humidity on the carbonyl species the following was observed. On Pt:SnO_2 PI the presence of water vapour strongly decreased the intensity of the Pt–CO bands, indicating a lower CO adsorption on the PtO_2 phase, which results in a lower level of CO oxidation on the PtO_2 phase. On the opposite, for the Pt:SnO_2 GI the intensity of the Pt–CO band is increased by the humidity, indicating a higher CO adsorption and hence an increased CO oxidation activity of the atomic Pt sites (in humid conditions). These findings suggest that the differences in the sensor performance (Fig. 1) are most likely related to the different chemical activity of the Pt sites.

4. Discussion

The Pt-structures, revealed by XAS, create new reaction sites in addition to the Sn–O–Sn sites present on undoped (pristine) SnO_2:

For Pt:SnO_2 GI the atomically distributed Pt offers new reactive surface sites (Pt–O–Sn), which separate the oxidation of CO from interfering compounds like water vapor.[13] While the pristine SnO_2 surface is deactivated by water vapour,[45] the Pt–O–Sn sites on Pt:SnO_2 remain active maintaining the sensing activity (Fig. 1). The increase of the carbonyl species in humid air can be explained by a decreased level of CO oxidation onto the (pristine) SnO_2 surface, which causes a shift for the surface reaction to the atomic Pt sites. This compensation of the decreased activity of SnO_2 surface explains the independence of the CO sensor signal from the water vapour in the background (Fig. 1).

For Pt:SnO_2 PI three different reactive sites are possible: the SnO_2 surface (Sn–O–Sn), the PtO_2 surface (Pt–O–Pt) or the boundary of the two oxides (Pt–O–Sn) and the gas phase, the so called 3-phase-boundary the latter one, the Pt–O–Sn site at the 3-phase-boundary, may differ from the Pt–O–Sn sites found for atomically distributed Pt.

Regarding the situation in dry air the operando DRIFT spectrum (Fig. 7a) suggests that the reaction is mainly taking place at the PtO_2 surface (Pt–O–Pt sites), indicated by the appearance of carbonyl species (2148 and 2131 cm^{-1}) and in line with the TPR XANES results, proving the feasible reduction and re-oxidation of the PtO_2 phase. Assuming that there is no electron exchange between SnO_2 and PtO_2, any reaction at the Pt–O–Pt sites does not change the resistance of SnO_2 and hence has no impact on the sensor signal. The CO oxidized on the PtO_2 phase is not anymore available for a reaction on the SnO_2 phase (Sn–O–Sn or Sn–O–Pt sites) and consequently the parallel reaction on the PtO_2 phase will decrease the sensor signals for a certain concentration, as it is observed for Pt:SnO_2 PI in dry air (Fig. 1). In humid air the situation changes: the carbonyl bands decrease strongly, *i.e.* the Pt–O–Pt sites deactivated, and the reaction is shifted to the SnO_2 surface or the 3-phase-boundary. As the pristine SnO_2 surface is deactivated in humid air, the oxidation of CO in humid air on Pt:SnO_2 PI has to take place at the Pt–O–Sn sites, *i.e.* the 3-phase-boundary. A reaction at the 3-phase-bouandary, which keeps the surface active in the presence of water vapour while the PtO_2 phase gets deactivated, gives an appropriate explanation for the high sensor performance of Pt:SnO_2 PI in humid air (Fig. 1).

5. Conclusions

By the use of complementary operando spectroscopic techniques – XAS and DRIFTS – and the direct comparison with analogous data of a related material, structure and surface chemistry of surface doped Pt:SnO_2 were revealed and provided the basis for better understanding of the CO gas sensing mechanism of Pt doped SnO_2. In contrast to atomically distributed Pt (gel-impregnation) it was found that introduced after the calcination step (powder-impregnation) Pt forms a separate oxide phase, which offers additional reaction sites, which are not electronically coupled to the SnO_2. Hence, the decreased sensor signals in dry air are caused by a parallel reaction on the PtO_2 phase with no effect onto the electrical properties of SnO_2. Nevertheless, the presence of PtO_2 clusters at the surface of SnO_2 prevents a complete deactivation of the SnO_2 surface in humid air, resulting in a higher CO sensing performance in the presence of water vapour.

This work demonstrated the fundamental role of structure and distribution of noble metals in oxide materials for the surface chemistry, which has a direct link to the materials functionality – in this case, gas sensing. Furthermore, it has been shown that the used of complementary experimental techniques and the comparison of rational designed materials is a powerful method to study the structure–function relationships of functional materials, such as gas sensors or catalysts.

Acknowledgements

We thank the ESRF (Grenoble) for beamtime allocation at beamline ID26 in the frame of proposal MA 1530 and the financial support.

References

1 A. Gurlo, N. Barsan and W. Udo, in *Metal Oxides – Chemistry and Applications*, ed. J. L. G. Fierro, CRC Press, 2006, pp. 683–738.
2 R. Jaaniso and O. Kiang Tan, *Semiconductor Gas Sensors*, Woodhead Publishing Limited, 2013.
3 A. Cabot, A. Diéguez, A. Romano-Rodriguez, J. R. Morante and N. Barsan, *Sens. Actuators, B*, 2001, **79**, 98–106.
4 D. Degler, H. W. P. De Carvalho, U. Weimar, N. Barsan, D. Pham, L. Mädler and J.-D. Grunwaldt, *Sens. Actuators, B*, 2015, **219**, 315–323.

5 A. Diéguez, A. Vilà, A. Cabot, A. Romano-Rodriguez, J. R. Morante, J. Kappler, N. Barsan, U. Weimar and W. Göpel, *Sens. Actuators, B*, 2000, **68**, 94–99.
6 M. Epifani, J. Arbiol, E. Pellicer, E. Comini, P. Siciliano, G. Faglia and J. R. Morante, *Cryst. Growth Des.*, 2008, **8**, 1774–1778.
7 G. Ghiotti, A. Chiorino, G. Martinelli and C. Carotta, *Sens. Actuators, B*, 1995, **25**, 520–524.
8 F. Gyger, A. Sackmann, M. Hübner, P. Bockstaller, D. Gerthsen, H. Lichtenberg, J.-D. Grunwaldt, N. Barsan, U. Weimar and C. Feldmann, *Part. Part. Syst. Charact.*, 2014, **31**, 591–596.
9 S. Harbeck, A. Szatvanyi, N. Barsan, U. Weimar and V. Hoffmann, *Thin Solid Films*, 2003, **436**, 76–83.
10 R. G. Pavelko, H. Daly, M. Hu, C. Hardacre and E. Llobet, *J. Phys. Chem. C*, 2013, **117**, 4158–4167.
11 T. Wagner, M. Bauer, T. Sauerwald, C. Kohl and M. Tiemann, *Thin Solid Films*, 2011, **520**, 909–912.
12 A. Marikutsa, M. Rumyantseva and A. Gaskov, *J. Phys. Chem. C*, 2015, **119**, 24342–24350.
13 K. Großmann, S. Wicker, U. Weimar and N. Barsan, *Phys. Chem. Chem. Phys.*, 2013, **15**, 19151–19158.
14 I. Kocemba and J. Rynkowski, *Sens. Actuators, B*, 2011, **155**, 659–666.
15 L. Mädler, T. Sahm, A. Gurlo, J.-D. Grunwaldt, N. Barsan, U. Weimar and S. Pratsinis, *J. Nanopart. Res.*, 2006, **8**, 783–796.
16 N. Murata, T. Suzuki, M. Kobayashi, F. Togoh and K. Asakura, *Phys. Chem. Chem. Phys.*, 2013, **15**, 17938.
17 N. Yamazoe, *Sens. Actuators, B*, 1991, **5**, 7–19.
18 N. Yamazoe, Y. Kurokawa and T. Seiyama, *Sens. Actuators, B*, 1983, **4**, 283–289.
19 J. Kappler, N. Barsan, U. Weimar, A. Dièguez, J. L. Alay, R. Rodriguez, J. R. Morante and W. Göpel, *Fresenius. J. Anal. Chem.*, 1998, **361**, 110–114.
20 A. Cabot, J. Arbiol, J. R. Morante, U. Weimar, N. Barsan and W. Gopel, *Sens. Actuators, B*, 2000, **70**, 87–100.
21 A. Gurlo and R. Riedel, *Angew. Chem., Int. Ed. Engl.*, 2007, **46**, 3826–3848.
22 N. Barsan, D. Koziej and U. Weimar, *Sens. Actuators, B*, 2007, **121**, 18–35.
23 M. Hübner, D. Koziej, J.-D. Grunwaldt, U. Weimar and N. Barsan, *Phys. Chem. Chem. Phys.*, 2012, **14**, 13249–13254.
24 D. Koziej, M. Hübner, N. Barsan, U. Weimar, M. Sikora and J.-D. Grunwaldt, *Phys. Chem. Chem. Phys.*, 2009, **11**, 8620–8625.
25 M. Hübner, D. Koziej, M. Bauer, N. Barsan, K. Kvashnina, M. D. Rossell, U. Weimar and J.-D. Grunwaldt, *Angew. Chem., Int. Ed. Engl.*, 2011, **50**, 2841–2844.
26 D. Koziej, K. Thomas, N. Barsan, F. Thibault-Starzyk and U. Weimar, *Catal. Today*, 2007, **126**, 211–218.
27 D. Koziej, N. Barsan, V. Hoffmann, J. Szuber and U. Weimar, *Sens. Actuators, B*, 2005, **108**, 75–83.
28 K. Großmann, R. G. Pavelko, N. Barsan and U. Weimar, *Sens. Actuators, B*, 2012, **166–167**, 787–793.
29 M. Hübner, D. Koziej, M. Bauer, N. Barsan, K. Kvashnina, M. D. Rossell, U. Weimar and J.-D. Grunwaldt, *Angew. Chem.*, 2011, **123**, 2893–2896.
30 M. Hübner, N. Barsan and U. Weimar, *Sens. Actuators, B*, 2012, **171–172**, 172–180.
31 N. Barsan and U. Weimar, *J. Phys.: Condens. Matter*, 2003, **15**, R813–R839.
32 B. Ravel and M. Newville, *J. Synchrotron Radiat.*, 2005, **12**, 537–541.
33 J. J. Rehr and R. C. Albers, *Rev. Mod. Phys.*, 2000, **72**, 621–654.
34 A. Russell and W. S. Epling, *Catal. Rev.: Sci. Eng.*, 2011, **53**, 337–432.
35 G. Ertl, *Angew. Chem., Int. Ed.*, 2008, **47**, 3524–3535.
36 M. D. Ackermann, T. M. Pedersen, B. L. M. Hendriksen, O. Robach, S. C. Bobaru, I. Popa, C. Quiros, H. Kim, B. Hammer, S. Ferrer and J. W. M. Frenken, *Phys. Rev. Lett.*, 2005, **95**, 255505.
37 E. M. C. Alayon, J. Singh, M. Nachtegaal, M. Harfouche and J. A. van Bokhoven, *J. Phys.: Conf. Ser.*, 2009, **190**, 012152.
38 B. L. M. Hendriksen and J. W. M. Frenken, *Phys. Rev. Lett.*, 2002, **89**, 046101.
39 J. Singh, M. Nachtegaal, E. M. C. Alayon, J. Stötzel and J. A. Van Bokhoven, *ChemCatChem*, 2010, **2**, 653–657.
40 E. M. C. Alayon, J. Singh, M. Nachtegaal, M. Harfouche and J. A. van Bokhoven, *J. Catal.*, 2009, **263**, 228–238.
41 A. Boubnov, A. Gänzler, S. Conrad, M. Casapu and J.-D. Grunwaldt, *Top. Catal.*, 2013, **56**, 333–338.
42 A. M. Gänzler, M. Casapu, A. Boubnov, O. Müller, S. Conrad, H. Lichtenberg, R. Frahm and J.-D. Grunwaldt, *J. Catal.*, 2015, **328**, 216–224.
43 J. Wintterlin, S. Väkening, T. V. W. Janssens, T. Zambelli and G. Ertl, *Science*, 1997, **278**, 1931–1934.
44 F. J. Gracia, L. Bollmann, E. E. Wolf, J. T. Miller and A. J. Kropf, *J. Catal.*, 2003, **220**, 382–391.
45 D. Degler, S. Wicker, U. Weimar and N. Barsan, *J. Phys. Chem. C*, 2015, **119**, 11792–11799.
46 E. Ivanova, M. Mihaylov, F. Thibault-Starzyk, M. Daturi and K. Hadjiivanov, *J. Mol. Catal. A: Chem.*, 2007, **274**, 179–184.